Journal of Biomedical Optics

BiomedicalOptics.SPIEDigitalLibrary.org

Monte Carlo simulations support non-Cerenkov radioluminescence production in tissue

Nicole L. Ackerman
Federico Boschi
Antonello E. Spinelli

SPIE.

Nicole L. Ackerman, Federico Boschi, Antonello E. Spinelli, "Monte Carlo simulations support non-Cerenkov radioluminescence production in tissue," *J. Biomed. Opt.* **22**(8), 086002 (2017), doi: 10.1117/1.JBO.22.8.086002.

Monte Carlo simulations support non-Cerenkov radioluminescence production in tissue

Nicole L. Ackerman,[a,*] Federico Boschi,[b] and Antonello E. Spinelli[c]
[a]Agnes Scott College, Department of Physics and Astronomy, Decatur, Georgia, United States
[b]University of Verona, Department of Computer Science, Verona, Italy
[c]San Raffaele Scientific Institute, Centre for Experimental Imaging, Department of Medical Physics, Milan, Italy

Abstract. There is experimental evidence for the production of non-Cerenkov radioluminescence in a variety of materials, including tissue. We constructed a Geant4 Monte Carlo simulation of the radiation from ^{32}P and ^{99m}Tc interacting in chicken breast and used experimental imaging data to model a scintillation-like emission. The same radioluminescence spectrum is visible from both isotopes and cannot otherwise be explained through fluorescence or filter miscalibration. We conclude that chicken breast has a near-infrared scintillation-like response with a light yield three orders of magnitude smaller than BGO. [DOI: 10.1117/1.JBO.22.8.086002]

Keywords: radioisotope luminescence imaging; Cerenkov; biomedical optics; imaging; Monte Carlo simulations.

Paper 170317R received May 16, 2017; accepted for publication Jul. 14, 2017; published online Aug. 17, 2017.

1 Introduction

Cerenkov imaging is a growing field with many clinical and preclinical applications, including preclinical radiopharmaceutical development, surface dosimetry during external-beam treatment, and endoscopy. First reported in small animal imaging systems in 2009,[1,2] Cerenkov imaging now has been observed in the clinic both from radiopharmaceuticals[3,4] and external beam treatment.[5]

In addition to utilizing the Cerenkov process directly, researchers have investigated coupling the Cerenkov-emitted light to other optical processes. For instance, Cerenkov light can be absorbed by quantum dots[6,7] or other fluorophores to either provide signal multiplexing[8] or convert the primarily blue light of the Cerenkov spectrum into red light, which has better tissue penetration.[9] Cerenkov light has been used as a source for photoactivated therapies, as it removes the need for an external light source.[10]

Another field, typically referred to as radioluminescence imaging, has emerged that similarly images optical light created by radiation, but which is not Cerenkov light or is in addition to Cerenkov light.[11] Usually, this involves introducing a scintillating material, which results in an increase of produced light.[12,13] This approach has been applied to microscopy[14] and preclinical imaging.[15,16]

Less has been published on radioluminescence that does not explicitly use scintillators. Outside of materials typically involved in measurements due to their scintillating properties, radioluminescence has been observed within biomedical contexts in air,[17] water,[18] tissue,[19] glass,[20] and plastic.[21] These materials are not typically referred to as "scintillators," but have radiation-excited luminescent (or fluorescent) properties. The radioluminescence of air, due to nitrogen, has been particularly well-studied since it is utilized in the measurement of cosmic rays.[22] Cerenkov light can only be produced by charged particles exceeding the speed of light in a given material (see Ref. 23 for a detailed physics description), but radioluminescence has no equivalent constraint and has been imaged from γ rays[24] and subthreshold α particles.[25]

In general, radioluminescence refers to light production caused by radiation interacting with a material, but we can identify two main categories of mechanisms other than Cerenkov light emission. The first is due to radiation exciting a molecule, which then emits light when returning to a lower energy level. This process would be referred to as fluorescence, delayed fluorescence, or phosphorescence based on the lifetime of the excited state. Scintillation refers to this type of process, typically within the context of detecting ionizing radiation.[26] A second possible mechanism is when the radiation ionizes molecules; the chemical reactions of these ions recombining or reacting could produce light in a process referred to as chemiluminescence.[27] The emission spectrum, lifetime, and intensity of light production through both of these mechanisms will depend on the molecules involved.

It is nontrivial to understand the processes that are responsible for the generation of light due to the interaction of radiation in a material. For instance, it has been shown that the apparent Cerenkov light produced from ^{111}In samples is due to ^{114}In impurities.[28] Similarly, Cerenkov light from ^{225}Ac is due to the β-emission of subsequent decays of daughter isotopes, not the ^{225}Ac decay itself.[28] In these cases, the apparent Cerenkov luminescence from liquid samples will not necessarily match observed emissions in animal models if the Cerenkov-emitting isotopes are not conjugated to the targeting molecules.[29] A separate example is the origin of light observed in bare plastic fibers used for proton beam dosimetry. While originally assumed to be due to Cerenkov light, it has been shown to be a scintillation response.[21] This is especially important, as the scintillation is proportional to dose while the Cerenkov emission is not.

*Address all correspondence to: Nicole L. Ackerman, E-mail: nackerman@agnesscott.edu

1083-3668/2017/$25.00 © 2017 SPIE

Monte Carlo simulations enable us to understand the underlying processes for radiation interactions, light generation, subsequent propagation, and detection. In addition to the previously described studies, many other reports have utilized Monte Carlo tools. An early study by Mitchell et al.[30] used Geant4[31] to investigate the inherent resolution of Cerenkov emission due to the extended particle path over which it is generated. Pagliazzi et al.[32] used Geant4 to generate Cerenkov photons from radionuclides and propagate photons through a realistic mouse tissue model in Molecular Optical Simulation Environment (MOSE).[33] Glaser et al.[34] utilized Geant4-based Architecture for Medicine-Oriented Simulations (GAMOS)[35] with a tissue optics model[36] to predict light fluence in tissue from external beams and radioisotopes. The same group, also using GAMOS, showed that Cerenkov light does not always provide an accurate measurement of dose, especially for proton beams.[37]

Radioluminescence has not been included in Monte Carlo models of Cerenkov light production in tissue in the past. Some required parameters have not been available for tissue, and it is difficult to interpret the existing experimental results. Deviations from the expected Cerenkov spectrum have been observed, but one possible explanation is miscalibrations in the filters of the imaging system.[28] The spectrum is also modulated by the wavelength-dependent absorption of tissue, notably due to hemoglobin, causing *in vivo* measurements to have significantly attenuated light for shorter wavelengths.[11] While these factors contribute, it is possible that there is a scintillation-like response that produces light in addition to the Cerenkov process.

The goal of this current work is to develop a unified Monte Carlo model, using the Geant4 toolkit, which includes both the production of Cerenkov and non-Cerenkov radioluminescence. Geant4 is an ideal framework due to its flexibility and rich physics models. However, it is typically utilized in situations where the materials and geometries are well-understood, such as modeling detector systems. Unfortunately, biological tissues typically have irregular shapes and varying physical properties. Not only may a single sample have varying densities and optical properties, but these important parameters will also vary from one sample to another. Hence, our focus is on the qualitative comparison between isotopes, distance from the source, and spectral intensities.

In this work, we show that a radioluminescence model based on scintillation provides a better match to the measured emission spectra of chicken breast exposed to radioactive sources. We consider possible modulations of the Cerenkov emission spectrum, including those due to optical properties and fluorescence, but none are able to explain an experimentally measured near-infrared (NIR) excess. We believe that these simulations results help clarify past experimental reports and can motivate further experimental studies. The scintillation yield needed to approximate the experimentally measured spectra can be included in future simulations.

2 Methods

2.1 *Experimental Measurements and Analysis*

Chicken breast samples were imaged in an IVIS Spectrum small animal optical imaging system (Perkin Elmer), as has been described in Ref. 20. In the center of the imaging field, we placed a 0.5-mL Eppendorf vial containing either 1 μCi of ^{99m}Tc-methylene diphosphate or 84 μCi adenosine 5'-triphosphate [γ-^{32}P]. ^{32}P is a β emitter with endpoint energy of 1710.66 keV, sufficient to produce Cerenkov light in tissue, whereas ^{99m}Tc is a γ emitter that is not expected to produce Cerenkov light.[20] A layer of black paper was added around the Eppendorf tube to block any light generated in the source. A slice of uniform chicken breast, 6-mm thick and 20-mm wide, was cut and placed ~5 mm from the radiation source. Spectral data were captured by using 18 20-nm bandpass filters, ranging from 500 to 840 nm. Each spectral image was generated from a 300-s exposure, with a binning of 16, f/1, and field of view of 6.6 cm.

The luminescence image was analyzed in Living Image 4.5 (Perkin Elmer) with the following corrections applied: dark background subtraction, flat field correction, cosmic correction, and lens distortion correction. The cosmic correction algorithm removes any signal spikes due to particles directly interacting with the CCD. Spectral data were captured for four ROIs (regions of interest), two corresponding to the tissue (signal) and two corresponding to background regions. The ROI locations are shown in Fig. 1. Note that the entire field of view is not shown and that the source is located at the edge of the image. For only the ^{99m}Tc images, a smoothing of 5×5 was applied.

Two additional measurements were performed without radioactive sources. We placed a sample of chicken breast in the IVIS system and acquired the luminescence spectrum, acquiring each filter for 300 s with binning of 16, f/1, and field of view of 13.6 cm. One corner of the chicken sample displayed a higher signal value, so one ROI was placed over this area, another ROI was placed over a different region of the chicken breast, and a third ROI was placed over a background region. We also captured the fluorescence spectra from the chicken breast sample using an excitation filter of 430 nm and the full set of 18 emission filters in the IVIS. For the fluorescence measurement, we used automatic (variable) acquisition times, a binning of 8, f/2, and field of view of 13.6 cm.

2.2 *Geant4 Simulation*

We constructed the simulation model using Geant4 version 10.02.p02.[31] The Penelope low-energy physics model was used for electromagnetic processes and the Cerenkov and scintillation processes were both enabled. The G4RadioactiveDecay process was used with the default settings of enabling the atomic relaxation module and internal conversion module. The tissue volume was constructed as a triangular prism with a thickness of 6.0 mm and a hypotenuse of 35.4 mm. The NIST material G4_MUSCLE_SKELETAL_ICRP, default density of 1.04 g/cm^3, provided the elemental composition of the chicken breast tissue. The radioactive source was modeled as a cylinder with a radius of 3.0 mm and a height of 11.0 mm, filled with liquid water. The liquid was surrounded by a layer of plastic (polypropylene) 0.8-mm thick. The optical properties of the plastic and water were not defined so that no photons would be generated in those materials. The center of the radioactive sample was placed 5.75 mm from the edge of the tissue sample to approximate the experimental setup. Radioactive decays of either ^{32}P or ^{99m}Tc (142.6832 keV excitation) were generated randomly in the water volume. Subsequent β decays of the long-lived ^{99}Tc ground-state were disabled.

The simulation results were written to two files. One file contained all energy deposits in the tissue material which were later processed to create dose maps. The second file recorded all photons that impacted a surface 0.1 mm above the top of the tissue. The photons' momentum vector, creation process, and location

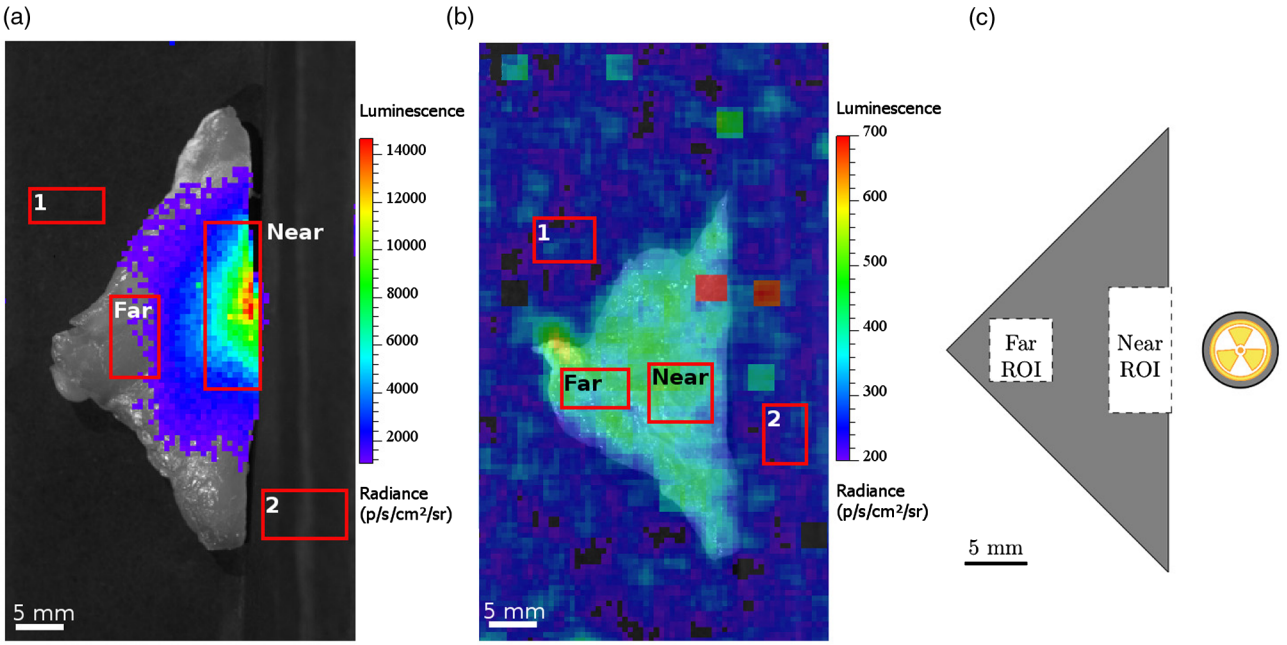

Fig. 1 ROIs for the experimental and simulation data. (a) Merged white light photograph and luminescence image for ^{32}P, 500-nm filter. (b) The merged photograph and luminescence image for ^{99m}Tc, for the 500-nm filter. (c) The geometry and ROIs as used in the simulation.

were all recorded for later processing. No imaging system was explicitly modeled, instead an angular threshold (30 deg) was applied to exclude photons that would not possibly reach a camera, while maintaining high statistics. Each simulation represents the detected photons from 100,000,000 decays of ^{32}P or 1,000,000,000 decays of ^{99m}Tc.

2.3 *Validation*

We validated the basic optical simulation and parameter conversion using two simple geometries and optical parameters, previously used by other techniques.[38–41] One model (hereafter referred to as model 1) used a 0.02-cm-thick slab with a width of 20 cm in each direction. The index of refraction of the slab was defined as 1.0, to match the index of the surrounding air. The absorption coefficient (μ_a) was set to 10.0 cm^{-1}, the scattering coefficient (μ_s) was set to 90.0 cm^{-1}, and the anisotropy (g) for the Henyey–Greenstein model was specified as $g = 0.75$. Photons were incident normal to the surface and reflected photons were counted for 5 runs of 1,000,000 events each. A second model (model 2) utilized a quasi-infinite geometry, with slab dimensions of 20 cm on each side. The same values of μ_a and μ_s were used, but with $n = 1.5$ and $g = 0$.

2.4 *Optical Parameters of Chicken Breast*

The optical properties of chicken breast were compared for different reported measurements. We identified four studies that measured μ_a and μ_s for chicken breast. Marquez et al.[42] used oblique-incidence reflectometry for wavelengths between 400 and 800 nm and investigated the differences based on muscle fiber orientations. The work of Honda et al.[43] focused on the changes in optical properties after laser treatment, but provided an untreated baseline from 350 to 1000 nm using the integrating-sphere technique. Adams et al.[44] also used the integrating-sphere technique to investigate optical properties responding to thermal changes, over a range of 500 to 1000 nm. Sun and Wang[45] also used oblique-incidence reflectometry but only considered a wavelength of 650 nm. Because the Geant4 model requires the parameters to be defined over the entire optical spectrum, this measurement cannot be used in the simulation.

All models are shown in Fig. 2, including the different muscle fiber orientations. Note that while Sun and Wang reports two measurements, corresponding to two fiber orientations, the difference is negligible on the scale of the plot, so only one is shown. The absorption coefficient is significantly higher in the Ref. 43 measurement, but all spectral measurements of μ_a show similar shapes. There is relatively good agreement between most measurements for μ_s, though Sun and Wang measure a significantly lower value.

In order to define the parameters in Geant4, we must convert the absorption coefficients to lengths and specify the spectra in terms of photon energy. The absorption length ℓ_a was calculated as the inverse of the absorption coefficient (μ_a)

$$\ell_a(\lambda) = \frac{1}{\mu_a(\lambda)}. \tag{1}$$

The standard Geant4 optical photon scattering process uses a double Henyey–Greenstein model.[46] The required parameters include the scattering length (defined as a function of energy) and single values for a forward scattering anisotropy constant (g_f), backward anisotropy constant (g_b), and a parameter f (between 0 and 1) that defines the relative fraction of the forward to backward model. While this parameterization is different from the typical Henyey–Greenstein model,[47] it simplifies to the traditional model if $g_f = g$ and f is set to 1.0. The published parameters are typically in terms of the reduced scattering coefficient μ_s', which can be converted to the scattering length (ℓ_s) by accounting for the anisotropy g

$$\ell_s(\lambda) = \frac{1-g}{\mu_s'(\lambda)}. \tag{2}$$

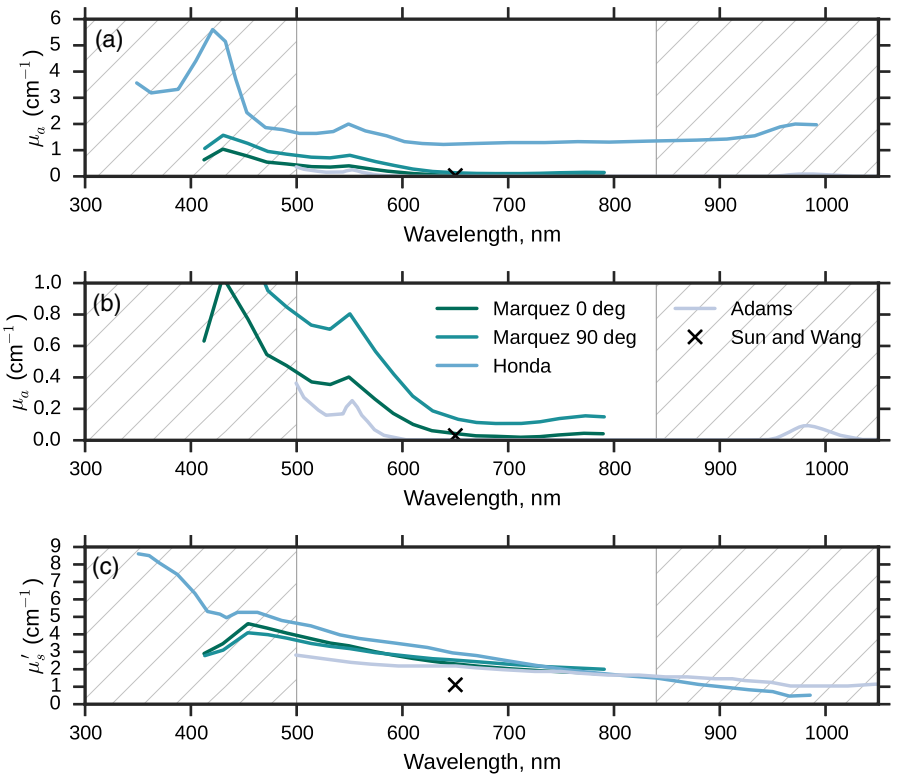

Fig. 2 Different optical parameters for chicken breast as reported in the literature. The hatched regions are outside the filters used in the IVIS. (a) All models for μ_a and (b) a view which better distinguishes the majority of models but excludes Honda et al.

Geant4 will kill a photon, or generate errors, if a photon enters a region in which the optical properties are not defined for its energy. In order to ensure that a consistent wavelength range was used (490 to 850 nm), any optical parameter data outside of the wavelength range was truncated. Data for the end points were generated by duplicating the values at the closest defined point. Geant4 used a spline model to generate values at intermediate points, except for the absorption length, where a linear interpolation was used to avoid unphysical negative values.

The index of refraction for chicken breast was reported in Sun and Wang as 1.397 ± 0.002 for the parallel orientation and 1.407 ± 0.003 for the vertical orientation. Marquez et al. reported an index of refraction of 1.37. The report of Sun and Wang was the only one to include a measured value for Mie anisotropy $g = 0.99$. Adams et al. used $g = 0.97$ and $n = 1.4$, though they state these are based on the measurements of Sun and Wang. In the simulation, we used $n = 1.37$ and $g = 0.99$.

2.5 *Analysis*

We typically present experimental measurements of emission spectra as fractional spectral components. The average radiance from the signal ROI (either near or far) was corrected by subtracting the average of the two background ROIs. The individual spectral values were normalized by dividing the sum of all values. Error bars are not shown on the measurements from ^{32}P due to the standard deviation being dominated by the variation in intensity over the near and far ROIs, as can be seen in Fig. 1. In order to compare the simulated spectra with the experimentally measured spectra, each simulated data point was centered on the IVIS filter value and included photons within ± 10 nm. The spectra were typically normalized to have an integral of 1. A second approach was to compare the ratio of the far to the near ROI for each wavelength. While the resulting shape is very unlike the actual detected spectrum, this cancels any individual filter miscalibrations. We defined the simulation ROIs to have similar sizes and placements to the ^{32}P experimental ROIs so that the changes in emission spectrum and intensity would be comparable.

We generated line profiles from the simulation and experimental data to quantify the spatial distribution of light, independent of spectrum. Experimental line profiles were calculated from an open-filter image in the Living Image software, using a line width of 2 pixels. Five lines were drawn with different orientations, each passing somewhere through the region of apparent maximum. The peak values of each line were aligned, corresponding to the edge, and then we calculated the mean and standard deviation for each position. We generated the line profiles for the simulation data by considering photons detected ± 1 pixel from the axis perpendicular to the edge and passing through the center of the source. A line profile of the simulated dose was similarly constructed by considering all energy deposits within the same ± 1 pixel region for all heights in the tissue.

2.6 *Generation of Radioluminescence in Geant4*

The radioluminescence process was modeled using the Geant4 scintillation method, which has been extensively used for modeling scintillating detectors.[48,49] In brief, scintillation light is generated in Geant4 based on the energy lost by a particle in a single step in a given material, where the material has a

characteristic light yield Y in terms of photons/MeV. The energy of the photons is generated based upon a user-entered spectrum, with an initial photon position that is uniform along the particle's path and with an isotropic direction. The number of photons varies based upon a Poisson distribution, with an optional broadening parameter needed for doped scintillator materials.[46]

The scintillation model requires an emission spectrum and yield, which have not been studied previously for chicken breast. Initially, we ran the simulation with a luminescence emission that is uniform in wavelength. This was used to observe the impact of the absorption and scattering parameters on the detected spectrum. Our IVIS measurements for ^{99m}Tc in chicken breast were used to estimate the radioluminescence spectrum. The average background signal for each wavelength was subtracted from the value measured in the near ROI to construct the signal spectrum ($\mathcal{L}_{\text{sig}}$). The simulated measurement in the near ROI ($\mathcal{L}_{\text{flat,out}}$) and signal spectra were both normalized to have a maximum value of one. A new luminescence spectrum $\mathcal{L}_{\text{in}}(\lambda)$, used in further simulations, was calculated by

$$\mathcal{L}_{\text{in}}(\lambda) = \frac{\mathcal{L}_{\text{sig}}(\lambda)}{\mathcal{L}_{\text{flat,out}}(\lambda)}. \quad (3)$$

3 Results

3.1 *Validation of Geant4 Optical Model*

Table 1 compares the simulation to past results for the two tested models. The measured reflectance in Geant4 is in good agreement, demonstrating the validity of the Geant4 optics models and our conversion process.

3.2 *Comparison of Chicken Breast Tissue Optical Parameters to Experimental Data*

Figure 3 shows the impact of the different tissue optical parameter models on the simulation results, when only a Cerenkov emission from ^{32}P is considered. In the near ROI, shown in (a), the Cerenkov spectrum from each of the models is in relatively good agreement with the experimentally measured ^{32}P data. In the far ROI, (b), each model shows a relatively similar shape for the light emitted, but the relatively intensity varies. All models predict less light at the far ROI than is measured, though the model of Adams et al. results in values most similar to the experimental measurement.

From Fig. 3(b), it appears that all models underestimate the light measured at farther distances. In conjunction with Fig. 2, this could be used to infer that μ_a for our sample was lower than these models predicted. In particular, Adams et al. note that their spectrophotometer and integrating sphere system is unable to provide accurate measurements of μ_a below 0.05 cm^{-1}. Another possibility is that this difference is due to the curvature of the tissue sample, which was not included in the simulation.

While no model correctly predicts the absolute ratio of light in the far to near ROIs, we can focus on the wavelength dependence of the ratio. The models have a similar trend, notably that short wavelengths are more attenuated at the far ROI than longer wavelengths. This trend is reflected in the experimental data, but the experimental and simulated results do not reflect the same trend for the longest wavelengths. The difference in shape in the NIR region in the far ROI will be addressed through introducing the radioluminescence model. For the subsequent simulations, we have used the optical parameters of Adams et al.

We ran additional simulations (results not shown) with variations on the model of Adams et al. We tested whether small changes in the anisotropy or index of refraction had a significant effect on the spectrum or relative light seen between near and far ROIs. No significant difference was seen between $g = 0.99$ and $g = 0.90$. Similarly, another simulation showed no significant difference for $n = 1.37$ versus $n = 1.4$.

Table 1 Validation of Geant4 optical model.

Source	Reflectance (model 1)	Reflectance (model 2)
MCML[38]	0.09734 ± 0.00035	0.25909 ± 0.00170
Giovanelli[39]		0.2600
Van de Hulst[40]	0.09739	
Prahl[41]	0.0971 ± 0.0003	0.2608 ± 0.0008
Geant4 (this work)	0.0972 ± 0.0003	0.2596 ± 0.0004

3.3 *Luminescence Spectrum from ^{99m}Tc*

Figure 4(a) shows the experimentally measured spectra from ^{99m}Tc in tissue and from the chicken breast with no radioactive sources present. The signal from ^{99m}Tc in chicken breast is low, but consistently above the diffuse background in the presence of ^{99m}Tc and above the background measured in chicken without a source present. The background signal (in the presence of ^{99m}Tc) is likely due to scattered light in air, demonstrating that blue light is more strongly scattered than NIR light. It is unlikely to be due to radiation interacting in air, given that one background ROI is much closer to the source [as shown in Fig. 1(b)] but the spectral signals are statistically equivalent. Compared to the luminescence measurement without ^{99m}Tc, the ^{99m}Tc-radiated chicken has a noticeable increase at both edges of the spectrum.

The γ decay of ^{99m}Tc is not expected to produce any Cerenkov emission, so the signal measured in Fig. 4(a) must be due to a non-Cerenkov radioluminescence process. While ^{99m}Tc has rare β decays, the decay probability is 10^{-5} for an endpoint energy of 436.3 keV and 2.6×10^{-5} for an endpoint energy of 346.7 keV,[50] rendering it unable to produce significant Cerenkov light. In 1,000,000,000 decays of ^{99m}Tc, no Cerenkov photons were produced in the simulation.

The dashed line in Fig. 4(b) shows the detected spectrum in the simulation, for a flat radioluminescence emission spectrum. The deviations largely correlate with the wavelength dependencies in the tissue optical parameters. The solid line shows the calculated emission spectrum, where a significant source of the fluctuations are statistical fluctuations in the experimental data.

Figure 5 shows the spectrum of the radioluminescence process from ^{99m}Tc after the near ROI has been used to estimate the needed emission spectrum. Because the near ROI was explicitly used to generate the radioluminescence emission, the agreement between experiment and simulation is not surprising. However, the far ROI provides a test of the optical parameters as the photons propagate through a greater distance of tissue.

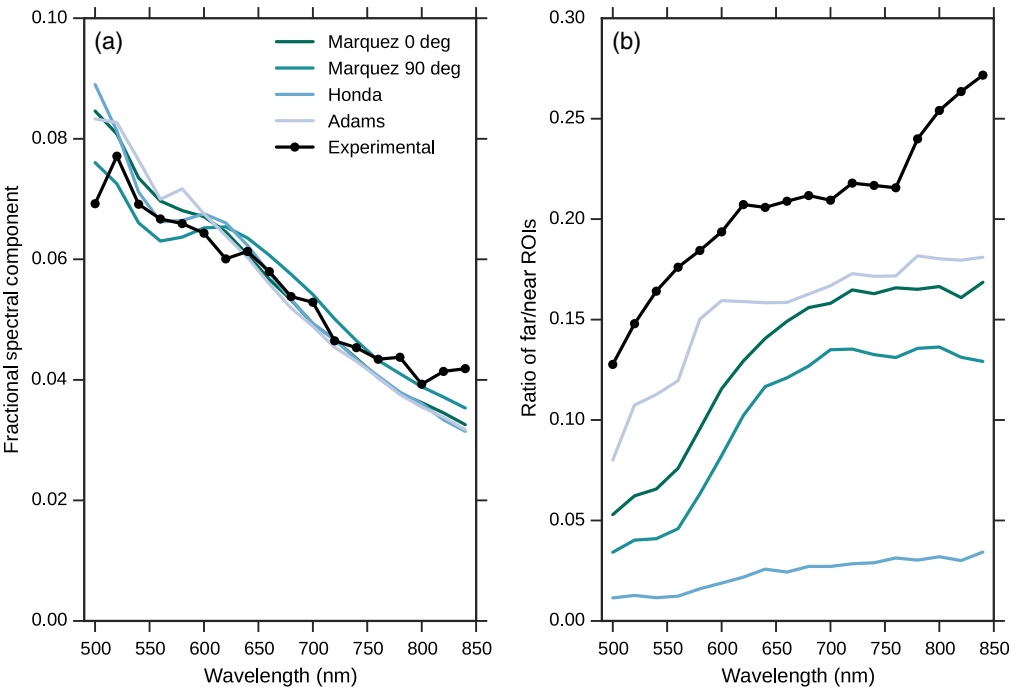

Fig. 3 (a) Spectral comparison between ^{32}P experimental results in the near ROI and the Cerenkov spectrum from different optical parameter models in the simulation. (b) The ratio of photons measured in the far ROI, compared to the near ROI, for the experimental measurement and the different optical models.

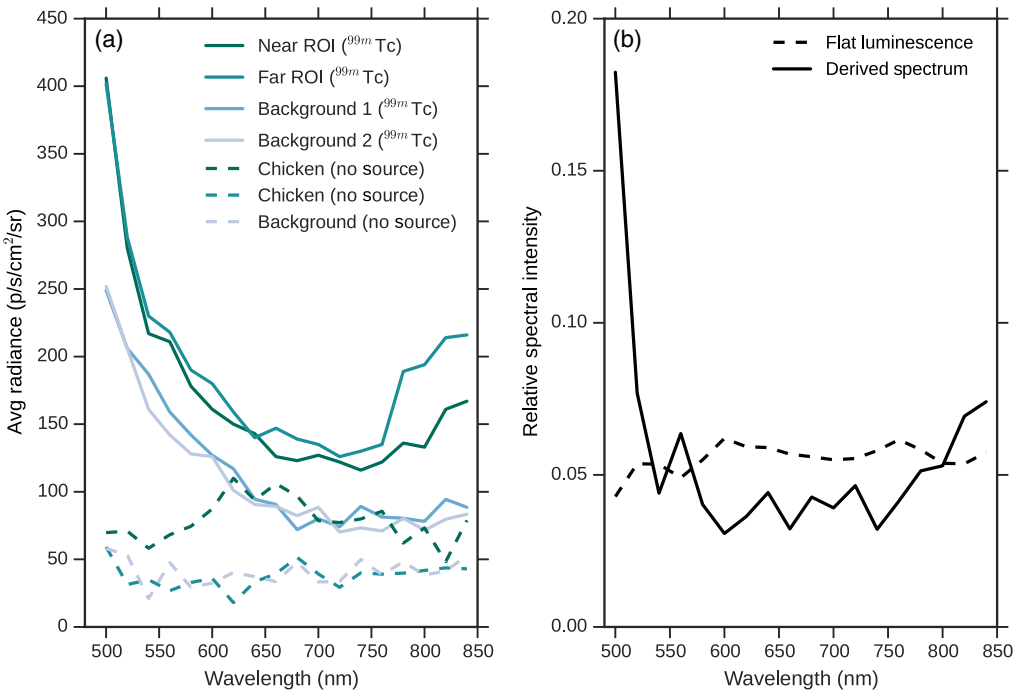

Fig. 4 Spectral profiles from ^{99m}Tc radioluminescence. (a) The experimentally measured luminescence spectra with and without the presence of ^{99m}Tc. Standard deviations on each measurement are 50 p/s/cm^2/sr. (b) The simulated spectrum that would be measured from a flat luminescence profile, and the calculated emission spectrum predicted to match the experimental spectrum (near ROI) shown in part (a).

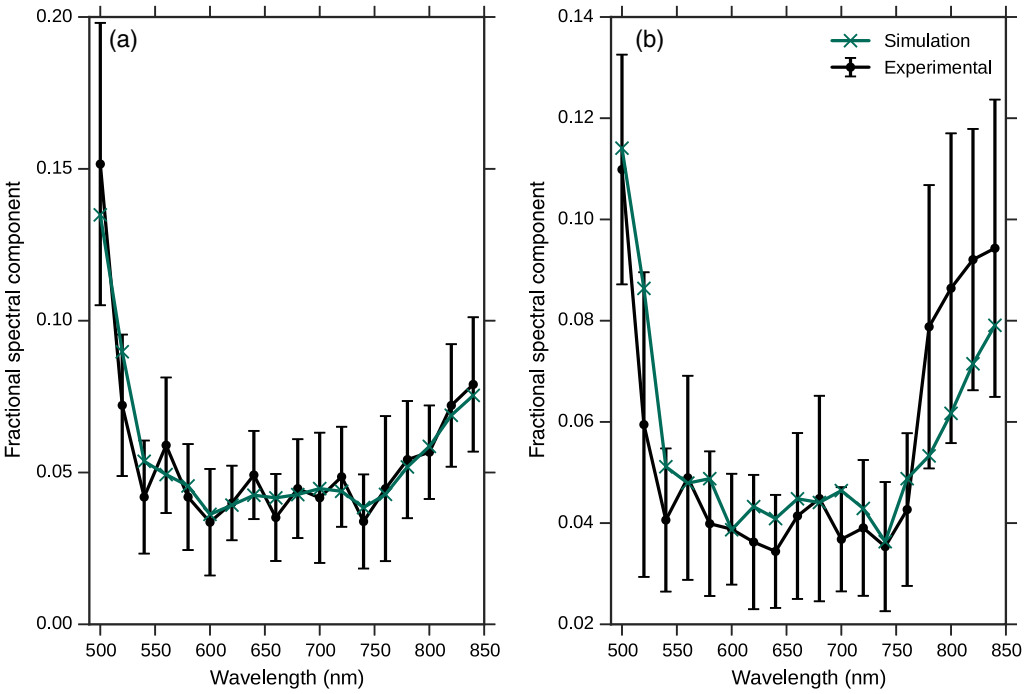

Fig. 5 The experimentally measured and simulation spectra from ^{99m}Tc using the optical properties of Adams et al. (a) The near ROI and (b) the far ROI. Error bars represent $\pm 1\sigma$, propagated from the standard deviation in the measured radiance.

3.4 *Fluorescence Spectrum of Chicken Breast*

Our measured emission from chicken breast from the 430-nm excitation is shown in Fig. 6. Multiple features are visible, with peaks around 520, 600, and 640 nm. This is largely in agreement with the turkey spectrum in Ref. 51, though their measurement used an excitation of 382 nm. Note that there is no significant emission in the NIR, which is expected due to the low autofluorescence from many tissue chromophores and other biological molecules in these wavelengths.[52]

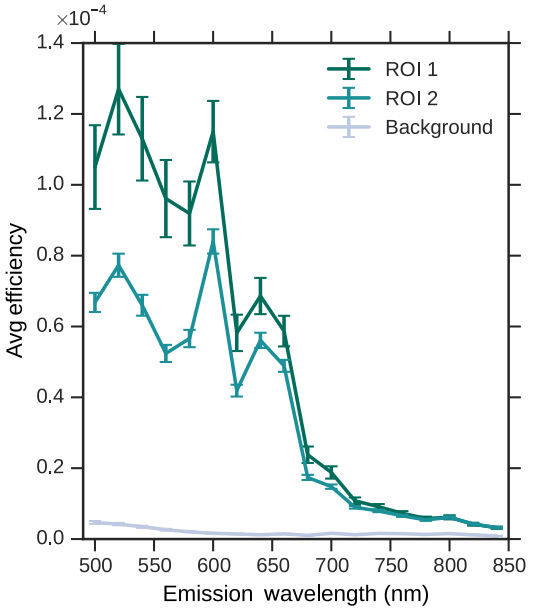

Fig. 6 Fluorescence of chicken breast with an excitation wavelength of 430 nm. The background corresponds to a region off the chicken breast while the two ROIs show the variation in one piece of tissue. Error bars are the standard deviation of the signal over the ROI.

3.5 *Spectral and Spatial Profiles for ^{32}P with Radioluminescence*

Figure 7 shows the experimental and simulation results for the spectral measurements in the near and far ROIs for decays of ^{32}P. The simulation model includes both Cerenkov light and the scintillation-based radioluminescence model. The scintillation yield parameter controls how many scintillation photons are generated, while the number of Cerenkov photons remains fixed. Hence, by varying the scintillation yield, we see a difference in the total simulated photon spectrum due to the differences in shapes of the two spectra. A yield of 0 photons/MeV corresponds to the detected spectrum from Cerenkov alone. While the 10 photons/MeV yield is a better match to the experimental data in the near ROI, it does not provide sufficient light in the NIR region of the far ROI. The 30 photons/MeV values overestimate the NIR contribution in the near ROI but are a better match in the far ROI.

Finally, Fig. 8 shows line profiles of light for an open filter image of ^{32}P. The simulation results show that the luminescence light falls off faster than the corresponding Cerenkov light, as shown in (a). The lateral plot shows that the detected light does not provide an accurate measure of the dose in the tissue, but it is important to remember that the dose is due to an external radiation source. Both the scintillation and Cerenkov light curves reflect a slower fall-off than the dose curve. The disagreement between simulated and experimental light measurements is likely due to the curvature of the chicken breast sample that is not reflected in the simulation geometry. Figure 8(b) compares the changes in overall shape (the curves are normalized to have the same area) due to different yield values for the scintillation

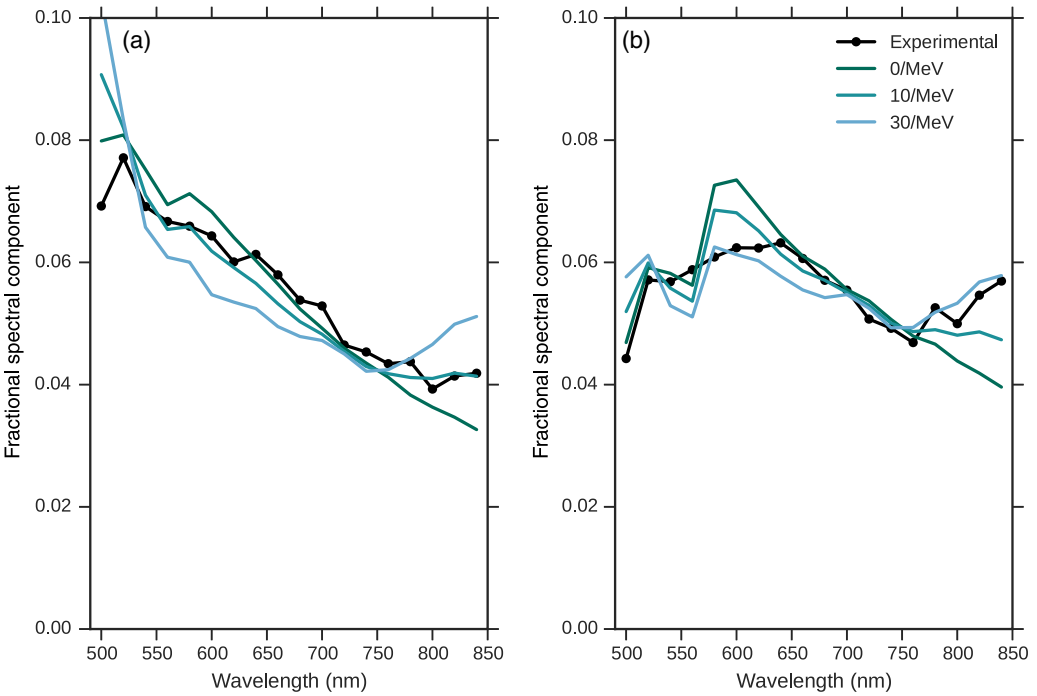

Fig. 7 Comparison of the measured spectrum from ^{32}P and the simulation results, for the near (a) ROI and far (b) ROI. The simulation results differ by the scintillation yield parameter used.

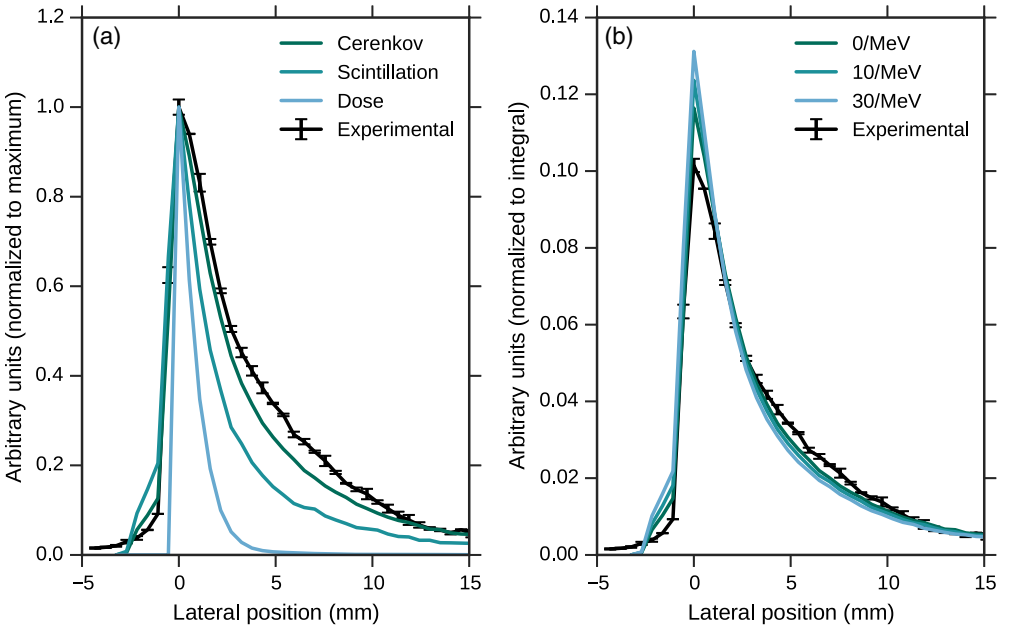

Fig. 8 Light intensity (open filter) as a function of position from the edge. Error bars represent $\pm\sigma$ from five similarly placed line profiles. (a) Comparison between different light production processes, dose, and experimental data. The curves are normalized to have the same maximum values. (b) The change in lateral profile due to varying the scintillation yield parameter, where the integral of each curve has been normalized to 1.

response. The changes are very small, indicating that the lateral light distribution is not an effective way to constrain the presence of a non-Cerenkov luminescence component.

4 Discussion and Conclusions

Our results support a scintillation-like radioluminescence emission from chicken breast. By using both ^{99m}Tc and ^{32}P experimental measurements, we show that this is a property of the tissue itself. In the case of ^{99m}Tc, there is no Cerenkov photon production process, so we can assume the entirety of the detected light is from the radioluminescence process. The dominant light production process due to ^{32}P is Cerenkov emission, but we are able to test the spectral impact of secondary processes. As we show in Fig. 7, a scintillation yield of

10 photons/MeV to 30 photons/MeV provides an improved spectrum in the longest wavelength region without disrupting the majority of the spectrum. We do not have the ability to provide a quantitative uncertainty because we do not have a good estimate of the experimental uncertainties. The variation in our spectral measurement is dominated by the change in intensity expected from geometry alone. Additionally, we do not have an independent confirmation of the filter calibrations, which could lead to small shifts in individual experimental data points.

Estimating the scintillation yield allows the radioluminescence process to be modeled in future Geant4 simulations, and it also provides an estimation of the emission intensity of this process. Scintillators have a yield 1000 times higher or more than our estimated photon yield: Bismuth Germanium Oxide (BGO) has a photon yield of 8500 photons/MeV and CsI(Tl) has a yield of 61,000 photons/MeV.[53] The physicochemical processes that produce this radioluminescence in chicken breast are possibly very different from the processes that produce photons in scintillator crystals, but we have referred to this radioluminescence as scintillation-like because that is the Geant4 model. It is worth noting that the spectral measurements taken with the IVIS should not be used as an absolute measurement of the radioluminescence emission spectrum. The Monte Carlo approach has allowed us to deconvolve the spectral changes due to absorption and scattering. However, the emission spectrum may have features that are not resolved due to the 20-nm-wide bandpass filters.

While we did measure the fluorescent spectra of chicken breast, the IVIS-based measurement is insufficient to include fluorescence (from photoexcitation) in the simulation in a meaningful way. The Geant4 fluorescence model is able to define a single absorption and emission spectrum per material, while tissue contains many different autofluorescent biomolecules with varying absorption and emission spectra. Additionally, the absorption spectrum would need to involve wavelengths below 500 nm. We know that the Cerenkov process generates photons below 500 nm, but we cannot define the tissue optical parameters below 500 nm using the model of Adams et al. nor make filter measurements below 500 nm.

An additional issue with the fluorescence model is that our measurement likely represents the surface fluorescence, not the bulk fluorescence of the chicken breast tissue. Fluorescence spectroscopy has been studied extensively in the meat industry, and the features we see are in agreement with a past study of lipid oxidation.[51] The same study showed that the fluorescence signal is not uniform throughout the volume. The resolution of the IVIS emission filters is insufficient to definitively identify the emission peaks, but the peaks we see are likely due to protoporphyrin IX,[54] metalloporphyrin,[55] or possibly riboflavin.[56] These complexes are degraded by past light exposure, further changing the fluorescence spectrum between the surface and internal bulk of the tissue.

Even without including an explicit fluorescence model in the Geant4 simulation, we can look for evidence of the fluorescence spectrum in the experimental data. We do not see the 600-nm peak from the fluorescence data reflected in the measured light from ^{32}P. While the ^{32}P spectrum shows a higher signal for the 520-nm filter compared to the 500-nm filter, comparison with the simulation shows that this may be due to a dearth of signal at 500 nm, rather than an excess at 520 nm. Additionally, our data show minimal fluorescent emission in NIR. While we cannot include fluorescence in our Geant4 model, we do not see any evidence in our data or the literature that the NIR emission is due to fluorescence from tissue absorbing blue light.

Should we be concerned about the disagreement between the simulation and experimental data for the 500-nm data point in the near ROI for ^{32}P? One possible issue is the large uncertainties in the data on which the radioluminescence spectral model is based. Another issue is that the chicken breast optical parameters of Adams et al. are only defined down to 500 nm. The 500-nm IVIS filter includes photons from 490 to 510 nm, so the simulation parameters are applied to the entire region but are based on half of this spectral region. However, we can see in Fig. 3 that all models, including those better defined in this spectral region, predict a higher signal in the 500-nm filter. We do not think that these concerns are as relevant to the NIR region, where the excess over the Cerenkov spectrum is seen for multiple filter values, both the near and far ROIs, and similarly for both ^{99m}Tc and ^{32}P.

Future experiments could help clarify the specific mechanism of radioluminescence, especially if carried out with equipment more specialized than the IVIS. Measuring a higher resolution radioluminescence spectrum could potentially identify the mechanism responsible, if the spectrum matched the emission of molecules known to be present in chicken breast tissue. It would also be helpful to excite the radioluminescence from an accelerator, rather than radioisotopes. This type of source could provide uniform dose at higher rates and potentially allow the measurement of radioluminescence lifetime, further identifying the process. Finally, our current experimental data are insufficient to test whether the radioluminescence is proportional to dose over a wide range of doses and for different incident particles. Future work should investigate this, as proportional radioluminescence production would enable imaging applications.

Simulation studies require a number of input parameters, which is especially challenging for biological tissues. Typically one must either rely upon published values or make a new measurement. This work has utilized a mix of these approaches. We may have had more accurate results had we directly measured the optical properties of the chicken breast used in the experiments. For two different chicken breast samples, Marquez et al.[42] showed that measurements of μ_s' varied by about 30% and μ_a' varied from 30% to 50%, while the overall spectral trends were preserved. However, high-quality measurements of absorption and scattering coefficients require specialized equipment. We believe it is more helpful to have generalizable qualitative results than a detailed model only applicable to one sample.

This work has evaluated chicken breast, but we expect that the scintillation-like radioluminescence process is common to many tissue types. Radioluminescence from ^{99m}Tc and ^{241}Am have already been reported in mice,[24,25] which indicates the light emission process may be common to all tissues, including human. While the light yield may be too small to enable *in vivo* clinical imaging, it may allow the direct imaging of radiolabeled human tumors after resection[57] for a wider variety of isotopes than Cerenkov imaging. Future imaging applications of radioluminescence can be studied through Monte Carlo simulation techniques, as we have demonstrated.

Disclosures

The authors have no conflicts of interest to report.

Acknowledgments

Dr. Ackerman acknowledges the support of the Julia T. Gary Science Fund and Dorothy Travis Joyner Faculty Innovation Fund at Agnes Scott College.

References

1. R. Robertson et al., "Optical imaging of Cerenkov light generation from positron-emitting radiotracers," *Phys. Med. Biol.* **54**, N355–N365 (2009).
2. A. E. Spinelli et al., "Cerenkov radiation allows in vivo optical imaging of positron emitting radiotracers," *Phys. Med. Biol.* **55**, 483–495 (2010).
3. A. E. Spinelli et al., "First human cerenkography," *J. Biomed. Opt.* **18**(2), 020502 (2013).
4. D. L. J. Thorek, C. C. Riedl, and J. Grimm, "Clinical Cerenkov luminescence imaging of 18f-FDG," *J. Nucl. Med.* **55**, 95–98 (2014).
5. R. Zhang et al., "Cherenkoscopy based patient positioning validation and movement tracking during post-lumpectomy whole breast radiation therapy," *Phys. Med. Biol.* **60**, L1 (2015).
6. R. S. Dothager et al., "Cerenkov radiation energy transfer (CRET) imaging: a novel method for optical imaging of pet isotopes in biological systems," *PLoS One* **5**, e13300 (2010).
7. F. Boschi and A. E. Spinelli, "Quantum dots excitation using pure beta minus radioisotopes emitting Cerenkov radiation," *RSC Adv.* **2**, 11049–11052 (2012).
8. H. Liu et al., "Radiation-luminescence-excited quantum dots for in vivo multiplexed optical imaging," *Small* **6**, 1087–1091 (2010).
9. X. Ma et al., "Enhancement of Cerenkov luminescence imaging by dual excitation of Er3+, Yb3+-doped rare-earth microparticles," *PLoS One* **8**, e77926 (2013).
10. C. Ran et al., "In vivo photoactivation without 'light': use of Cherenkov radiation to overcome the penetration limit of light," *Mol. Imaging Biol.* **14**(2), 156–162 (2012).
11. A. E. Spinelli and F. Boschi, "Novel biomedical applications of Cerenkov radiation and radioluminescence imaging," *Phys. Med.: Eur. J. Med. Phys.* **31**, 120–129 (2015).
12. F. Boschi et al., "Combined optical and single photon emission imaging: preliminary results," *Phys. Med. Biol.* **54**(23), L57 (2009).
13. M. T. King et al., "Beta-radioluminescence imaging: a comparative evaluation with Cerenkov luminescence imaging," *J. Nucl. Med.* **56**, 1458–1464 (2015).
14. G. Pratx et al., "Radioluminescence microscopy: measuring the heterogeneous uptake of radiotracers in single living cells," *PLoS One* **7**, e46285 (2012).
15. A. E. Spinelli, C. R. Gigliotti, and F. Boschi, "Unified approach for bioluminescence, Cerenkov, beta, X and γ rays imaging," *Biomed. Opt. Express* **6**, 2168–2180 (2015).
16. M. T. King et al., "Flexible radioluminescence imaging for FDG-guided surgery," *Med. Phys.* **43**, 5298–5306 (2016).
17. B. Fahimian et al., "Seeing the invisible: direct visualization of therapeutic radiation beams using air scintillation," *Med. Phys.* **41**(1), 010702 (2014).
18. M. D. Tarasov et al., "Efficiency of radioluminescence of water under the action of accelerated electrons," *Instrum. Exp. Tech.* **50**, 761–763 (2007).
19. A. E. Spinelli et al., "Optical imaging of Tc-99m-based tracers: in vitro and in vivo results," *J. Biomed. Opt.* **16**(11), 116023 (2011).
20. M. Pagliazzi, F. Boschi, and A. E. Spinelli, "Imaging of luminescence induced by beta and gamma emitters in conventional non-scintillating materials," *RSC Adv.* **4**, 13687–13692 (2014).
21. A. Darafsheh et al., "The visible signal responsible for proton therapy dosimetry using bare optical fibers is not Cerenkov radiation," *Med. Phys.* **43**, 5973–5980 (2016).
22. M. Nagano et al., "New measurement on photon yields from air and the application to the energy estimation of primary cosmic rays," *Astropart. Phys.* **22**, 235–248 (2004).
23. E. Ciarrocchi and N. Belcari, "Cerenkov luminescence imaging: physics principles and potential applications in biomedical sciences," *EJNMMI Phys.* **4**, 14 (2017).
24. F. Boschi et al., "Small-animal radionuclide luminescence imaging of thyroid and salivary glands with Tc99m-pertechnetate," *J. Biomed. Opt.* **18**(7), 076005 (2013).
25. F. Boschi et al., "Optical imaging of alpha emitters: simulations, phantom, and in vivo results," *J. Biomed. Opt.* **16**(12), 126011 (2011).
26. G. F. Knoll, *Radiation Detection and Measurement*, John Wiley & Sons, New York (2010).
27. G. M. Barenboĭm, A. N. Domanskiĭ, and K. K. Turoverov, *Luminescence of Biopolymers and Cells*, Springer, New York (1969).
28. B. J. Beattie et al., "Quantitative modeling of Cerenkov light production efficiency from medical radionuclides," *PLoS One* **7**, e31402 (2012).
29. N. L. Ackerman and E. E. Graves, "The potential for Cerenkov luminescence imaging of alpha-emitting radionuclides," *Phys. Med. Biol.* **57**, 771–783 (2012).
30. G. S. Mitchell et al., "In vivo Cerenkov luminescence imaging: a new tool for molecular imaging," *Philos. Trans. Ser. A, Math., Phys. Eng. Sci.* **369**, 4605–4619 (2011).
31. S. Agostinelli et al., "Geant4-a simulation toolkit," *Nucl. Instrum. Methods Phys. Res., Sect. A* **506**, 250-303 (2003).
32. M. Pagliazzi et al., "Development of a simulation environment for Cerenkov luminescence imaging," in *IEEE Nuclear Science Symp. and Medical Imaging Conf. (NSS/MIC '13)*, pp. 1–6 (2013).
33. S. Ren et al., "Molecular optical simulation environment (MOSE): a platform for the simulation of light propagation in turbid media," *PLoS One* **8**, e61304 (2013).
34. A. K. Glaser et al., "Cherenkov radiation fluence estimates in tissue for molecular imaging and therapy applications," *Phys. Med. Biol.* **60**, 6701–6718 (2015).
35. P. Arce et al., "GAMOS: a framework to do Geant4 simulations in different physics fields with an user-friendly interface," *Nucl. Instrum. Methods Phys. Res., Sect. A* **735**, 304–313 (2014).
36. A. K. Glaser et al., "A GAMOS plug-in for GEANT4 based Monte Carlo simulation of radiation-induced light transport in biological media," *Biomed. Opt. Express* **4**, 741–759 (2013).
37. A. K. Glaser et al., "Optical dosimetry of radiotherapy beams using Cherenkov radiation: the relationship between light emission and dose," *Phys. Med. Biol.* **59**(14), 3789–3811 (2014).
38. L. V. Wang and H.-I. Wu, *Biomedical Optics: Principles and Imaging*, John Wiley & Sons, Hoboken, New Jersey (2007).
39. R. Giovanelli, "Reflection by semi-infinite diffusers," *J. Mod. Opt.* **2**(4), 153–162 (1955).
40. H. C. Van de Hulst, *Multiple Light Scattering: Tables, Formulas, and Applications*, Academic Press, New York (1980).
41. S. A. Prahl et al., "A Monte Carlo model of light propagation in tissue," in *Dosimetry of Laser Radiation in Medicine and Biology*, G. Mueller and D. Sliney, Eds., pp. 102–111, SPIE Press, Bellingham, Washington (1989).
42. G. Marquez et al., "Anisotropy in the absorption and scattering spectra of chicken breast tissue," *Appl. Opt.* **37**, 798–804 (1998).
43. N. Honda et al., "Determination of optical property changes by laser treatments using inverse adding-doubling method," *Proc. SPIE* **7175**, 71750Q (2009).
44. M. T. Adams et al., "Thermal dose dependent optical property changes of ex vivo chicken breast tissues between 500 and 1100 nm," *Phys. Med. Biol.* **59**(13), 3249–3260 (2014).
45. P. Sun and Y. Wang, "Measurements of optical parameters of phantom solution and bulk animal tissues in vitro at 650 nm," *Opt. Laser Technol.* **42**, 1–7 (2010).
46. Geant Collaboration, "Physics reference manual," 2015, http://geant4.web.cern.ch/geant4/G4UsersDocuments/UsersGuides/PhysicsReferenceManual/html/PhysicsReferenceManual.html (10 April 2017).
47. L. G. Henyey and J. L. Greenstein, "Diffuse radiation in the galaxy," *Astrophys. J.* **93**, 70–83 (1941).
48. S. Riggi et al., "Geant4 simulation of plastic scintillator strips with embedded optical fibers for a prototype of tomographic system," *Nucl. Instrum. Methods Phys. Res., Sect. A* **624**, 583–590 (2010).
49. S. Lo Meo et al., "A Geant4 simulation code for simulating optical photons in SPECT scintillation detectors," *J. Instrum.* **4**(07), P07002 (2009).
50. M. M. Bé et al., *Table of Radionuclides (Vol. 1-A= 1 to 150)*, Vol. **1**, Bureau International des Poids et Mesures, Sèvres, France (2004).
51. A. Veberg et al., "Measurement of lipid oxidation and porphyrins in high oxygen modified atmosphere and vacuum-packed minced turkey and pork meat by fluorescence spectra and images," *Meat Sci.* **73**, 511–520 (2006).

52. S. Achilefu, "The insatiable quest for near infrared fluorescent probes for molecular imaging," *Angew. Chem.* **49**, 9816–9818 (2010).
53. M. Moszynski et al., "Absolute light output of scintillators," *IEEE Trans. Nucl. Sci.* **44**, 1052–1061 (1997).
54. S. Bagdonas et al., "Phototransformations of 5-aminolevulinic acid-induced protoporphyrin IX in vitro: a spectroscopic study," *Photochem. Photobiol.* **72**, 186–192 (2000).
55. J. Wakamatsu, T. Nishimura, and A. Hattori, "A Zn-porphyrin complex contributes to bright red color in Parma ham," *Meat Sci.* **67**, 95–100 (2004).
56. J. P. Wold et al., "The role of naturally occurring chlorophyll and porphyrins in light-induced oxidation of dairy products. A study based on fluorescence spectroscopy and sensory analysis," *Int. Dairy J.* **15**, 343–353 (2005).
57. A. E. Spinelli et al., "Cerenkov and radioluminescence imaging of brain tumor specimens during neurosurgery," *J. Biomed. Opt.* **21**(5), 050502 (2016).

Nicole L. Ackerman received her SB degree in physics from Massachusetts Institute of Technology in 2007 and her PhD in physics from Stanford University in 2013. She is an assistant professor of physics at Agnes Scott College, Decatur, Georgia, USA. Her main research areas are using Geant4 for Cerenkov imaging and microdosimetry.

Federico Boschi received his PhD from the University of Verona in 2008 and is now a researcher at the Optical Imaging Laboratory, University of Verona. Before his PhD, he was involved in different research activities in astrophysics and he switched to preclinical imaging working with small animal MR and optical imaging in 2004. His main research areas are Cerenkov and radioluminescence imaging, *in vivo* optical imaging using nanoparticles, and small animal magnetic resonance imaging.

Antonello E. Spinelli received his PhD in medical physics from the Institute of Cancer Research, University of London, UK, in 2004, and the medical physics expert degree from the University of Bologna, in 2009. He is the small animal optical imaging research coordinator of the San Raffaele Scientific Institute, Milan, Italy. His main research areas are *in vivo* optical imaging, Cerenkov and radioluminescence imaging, and preclinical CT imaging.